

Low-Threshold Amplified Spontaneous Emission in Blue Quantum Dots Enabled by Effectively Suppressing Auger Recombination

Sheng Wang, Jiahao Yu, Haiqiao Ye, Mingbo Chi, Heng Yang, Haihui Wang, Fan Cao, Wenqiang Li, Lingmei Kong, Lin Wang, Rui Chen,* and Xuyong Yang*

The amplified spontaneous emissions in blue quantum dots (QDs) are still constrained by their high thresholds due to the challenge in engineering alloyed core–shell interface in the QDs with a wide bandgap to suppress Auger recombination. Compared with their red and green counterparts, the larger reactivity difference between the alloyed shell precursors makes it hard to regulate the composition and structure of the shell, and the smaller potential barrier between the core and the alloyed shell in blue QDs renders charge carriers tunneling into surface defects easier. Here, we employ a Lewis soft base ligand, 1-decanethiol, to balance the mismatched reactivity between Zn and Cd precursors for crafting a thick gradient alloyed shell with gradually increased potential barrier, which can not only restrict the charge carriers tunneling but also smooth the confinement potential. As a result, the resulting blue QDs show a long Auger lifetime of 1.3 ns, and a low threshold of $6.9 \mu\text{J cm}^{-2}$ excited by a femtosecond laser, which is the record value among all reported blue-emitting nanocrystals and comparable to those of state-of-the-art red and green QDs.

spectral tunability and solution processability.^[1–5] Currently, the low-threshold ASE of several $\mu\text{J cm}^{-2}$ based on green and red QDs have been demonstrated,^[6,7] yet the development of that in the blue region still lags far behind, thereby retarding the applications ranging from full-color laser displays to high-density photomemories.^[8] In general, to obtain blue emission, small-size QDs with stronger quantum confinement are required.^[9] The finite size, however, aggravates the undesired nonradiative Auger recombination (AR), which is responsible for the degradation of population inversion and induces the increase of ASE threshold.^[10–12]

Substantial efforts have been devoted to mitigating AR process in QDs.^[13–17] Strikingly, Cragg et al. theoretically predicted that the AR rate in QDs can be diminished for over three orders of magnitude

1. Introduction

Semiconductor quantum dots (QDs) are regarded as promising optical gain media for amplified spontaneous emission (ASE) and lasing due to their narrow emission linewidths, wide range

by smoothing the confinement potential between the core and the shell materials.^[18,19] Subsequently, Demir et al. reported a low threshold of $\approx 50 \mu\text{J cm}^{-2}$ in blue-emitting QDs by utilizing a femtosecond laser to pump ZnCdS/ZnS core/shell QDs with an unintentionally thin alloyed interface.^[20,21] However, it is still a great challenge to manipulate the alloyed interface in blue QDs to further reduce the ASE threshold. When compared to green and red QDs, the alloyed interface engineering in blue QDs suffers from two issues: first, due to the relative small energy band offset between the core and the shell, the formation of intermediated alloyed shells would relax the quantum confinement and result in more frequent interactions between the core-localized electrons and holes with the surface traps. Second, the engineering of ZnCdS alloyed shell in blue ZnCdS/ZnS QDs is more difficult than the case of CdSSe alloyed shell in red CdSe/CdS QDs, because the reactivity difference between Zn and Cd precursors is much larger than that between S and Se precursors.^[22] When ZnCdS shell is deposited on the QD core, the rapid formation of CdS-rich phase leads to the non-uniform circumferential composition distribution, which disorders the alloyed shell structure and is detrimental to the regulation of the potential shape.^[22,23]

Here, we report an elaborate reactivity balance strategy to fabricate the intermediated alloyed structure in blue QDs, which enables a record low threshold in all blue-emitting QDs. According to “hard and soft acids and bases (HSAB) rule”,

Dr. S. Wang, H. Ye, H. Yang, H. Wang, F. Cao, W. Li,
L. Kong, Dr. L. Wang, Prof. X. Yang
Key Laboratory of Advanced Display and System Applications
of Ministry of Education
Shanghai University
149 Yanchang Road, Shanghai 200072, China
E-mail: yangxy@shu.edu.cn

J. Yu, Prof. R. Chen
Department of Electrical and Electronic Engineering
Southern University of Science and Technology
Shenzhen, Guangdong 518055, China
E-mail: chenr@sustech.edu.cn

Dr. M. Chi
State Key Laboratory of Applied Optics
Changchun Institute of Optics, Fine Mechanics and Physics
Chinese Academy of Sciences
Changchun 130033, China

The ORCID identification number(s) for the author(s) of this article can be found under <https://doi.org/10.1002/adom.202100068>.

DOI: 10.1002/adom.202100068

1-decanethiol (DCT), a Lewis soft base ligand, has more affinity to Cd^{2+} ions (soft acid) than Zn^{2+} ions (borderline acid), which reduces the reactivity of Cd precursor and relieves the reactivity difference between Cd and Zn precursors.^[24,25] Benefiting from the well-matched reactivity of precursors, the thick gradient alloyed shell is achieved through the layer-by-layer growth. The thick shell with a gradual increased potential barrier provides both the large charge tunneling barrier and the smooth confinement potential. As a result, the resulting blue QDs with a thick gradient alloyed shell demonstrate a very low ASE threshold of $6.9 \mu\text{J cm}^{-2}$ under excitation by a femtosecond laser.

2. Results and Discussion

The growth kinetics of multi-component alloy materials is dependent on the relative reactivity between precursors.²⁵ To achieve the blue QDs with alloyed shell, DCT, an alkane thiol, is employed as the sulfur precursor and the reactivity-controlling ligand. Based on the HSAB rule, the affinity between DCT ligand and Cd-OA is stronger than that between DCT and Zn-OA (soft acid, with $\text{Cd}^{2+} > \text{Zn}^{2+}$). Consequently, the strong coordination will form more stable compounds to limit Cd^{2+} reactivity. To evaluate the relative reactivity, the elemental compositions of ZnCdS QDs prepared by DCT and trioctylphosphine sulfide (TOPS), respectively, are determined by X-ray photoelectron spectroscopy (XPS) (Figure S1, Supporting Information). Compared to traditional TOPS-prepared ZnCdS QDs, the molar ratios of Zn/Cd in DCT-prepared ZnCdS QDs are much closer to the precursor feeding molar ratio of 1:1, which confirms that the reactivity difference between Zn and Cd precursors is effectively mitigated by DCT ligand and thus enables the structure regulation of the alloyed shell.

We repeatedly inject the calculated amount of Cd-OA and DCT at an elevated temperature (310 °C) into a reaction flask containing ZnCdS cores and excess Zn-OA for the layer-by-layer growth of alloyed shell. The outer ZnS shell is subsequently deposited by adding the mixture of Zn-OA and DCT (Figure 1a). The Zn-OA in the reaction system not only provides Zn source but also inhibits QDs ripening during the shell growth. The morphology evolution of C/GA/S QDs is shown in Figure 1b. All samples exhibit monodispersed spheres with gradually increasing diameters from the original ZnCdS core (5.7 nm) to the final core/shell QDs (14.0 nm). The thicknesses of the alloyed shell and ZnS shell are estimated to be ≈ 3.2 and ≈ 0.9 nm, corresponding to 10 and 3 monolayers, respectively. For unveiling the influence of the shell structure on ASE performance, the reference C/S and C/HA/S QDs with identical sizes are used to rule out the effect of the volume on Auger decay (Figures S2–S4, Supporting Information).

The shell structure determines the confinement potential shape and plays a vital role in the regulation of Auger decay and lattice tension. With the increase of the shell thickness, all samples remain wurtzite phase without phase transformation, and the magnitudes of the shift of diffraction peaks are dependent on their shell compositions (Figure 1c and Figure S5, Supporting Information). Raman spectroscopy is a very sensitive technique for the detection of the internal structure including interface alloying and structural defects.^[26] As shown in Figure 2a,

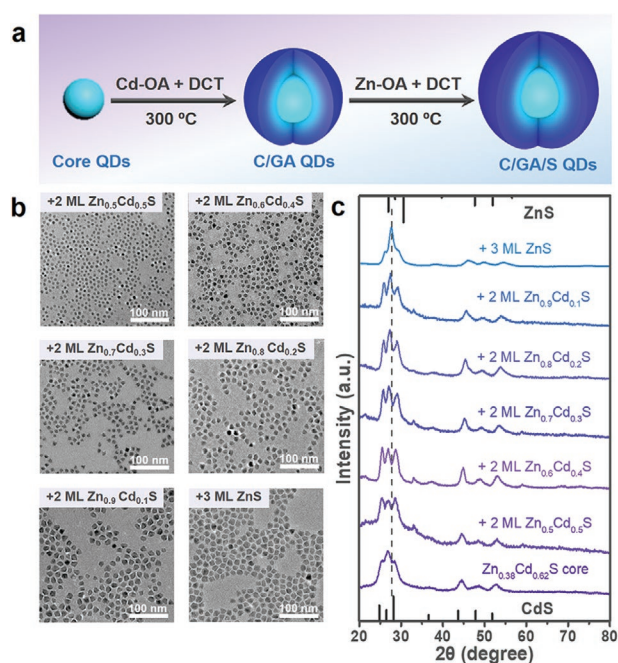


Figure 1. a) Schematic illustration of the synthesis process of C/GA/S QDs. Temporal evolution of b) TEM images and c) XRD patterns of C/GA/S QDs upon shell growth.

$\text{Zn}_{0.38}\text{Cd}_{0.62}\text{S}$ cores present distinctive peaks at 310 cm^{-1} and around 603 cm^{-1} , which corresponds to 1-LO (longitudinal optical) and 2-LO phonon mode, respectively, keeping in accordance with previous reports.^[27,28] With the deposition of the initial four ZnS monolayers, the LO phonon modes of C/S QDs gradually shift to higher energy owing to the interface alloying. As ZnS shell is further deposited, the shift of the phonon mode can be negligible. This result indicates that the unintentional alloying process only occurs within a finite interface region and therefore, has limited effect on the regulation of confinement potential (Figure S6, Supporting Information). By contrast, with the increase in the alloyed shell thickness, the 1-LO phonon modes keep fixed in C/HA/S QDs and red-shifted in C/GA/S QDs, respectively, which provides conclusive evidences for the formation of homogeneous and gradient alloyed shell (Figure S7, Supporting Information, and Figure 2a). Moreover, the ZnS shell has a smaller lattice constant than the $\text{Zn}_{0.38}\text{Cd}_{0.62}\text{S}$ core, and the accumulated interface strain will induce the lattice defects and distinctly broaden the Raman linewidths. Compared with the reference C/S and C/HA/S QDs, the linewidths of 1-LO phonon modes of C/GA/S QDs maintain narrow consistently, which reveals that the gradient alloyed shell can significantly release the interface lattice misfit strain and reduce the lattice defect density (Figure 2b). The defect density is further estimated by adopting the space-charge-limited current (SCLC) measurement, which is performed with the device configuration of indium tin oxide/1,3,5-tris(1-phenyl-1H-benzimidazol-2-yl)benzene (TPBi)/QDs/TPBi/lithium fluoride/Al (Figure S8, Supporting Information). The trap state density (N_t) is determined by the trap-filled-limit voltage (V_{TFL}) according to the following equation:

$$N_t = \frac{2V_{TFL}\epsilon\epsilon_0}{qL^2} \quad (1)$$

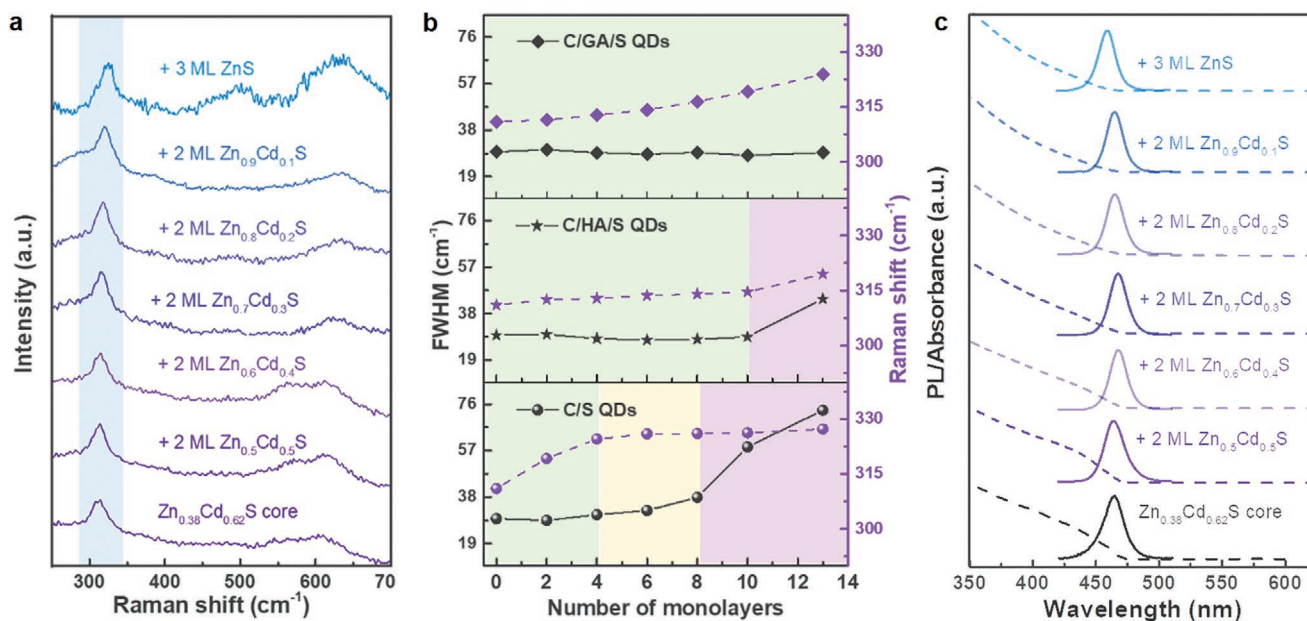


Figure 2. Evolution of a) Raman spectra of C/GA/S QDs, b) FWHMs and spectral shifts of the 1-LO phonon modes of the three types of QDs, and c) absorption and PL spectra of C/GA/S QDs.

where V_{TFL} is the onset voltage of the TFL region, L is the thickness of the QD emissive layer. ϵ_0 is the vacuum permittivity, and ϵ is the relative dielectric constant of QDs. The N_i of C/S, C/HA/S and C/GA/S QDs is gradually decreased and estimated to be 2×10^{16} , 1.5×10^{16} , and 1.3×10^{16} cm⁻³, respectively.

The shell growth process is also monitored by photoluminescence (PL) and absorption spectra (Figure 2c). The obtained PL spectra of the three types of QDs show narrow full width at half maximum (FWHM) of 18–20 nm, as evidenced by the uniform morphologies. Due to the different shell structures, the evolutions of spectral shifts are obviously distinctive. The spectra of C/S QDs systematically are shifted toward the short wavelength direction (Figure S9a, Supporting Information), resulting from the increased bandgap caused by the inward diffusion of Zn ions from ZnS shell into ZnCdS cores at high temperatures. In contrast, the spectral redshifts in C/HA/S QDs (Figure S9b, Supporting Information) are stemmed from the enhanced delocalization of carriers, due to the small potential offset between the core and the homogeneous alloyed shell. However, in the case of C/GA/S QDs, the gradually increased confinement potential in the alloyed shell enables the PL peak position almost immobile. The PLQYs of C/S, C/HA/S and C/GA/S, QDs are 78%, 36%, and 62%, respectively. Combining with the results of SCLC, Raman, and transient PL measurements (Figure S10, Supporting Information), it is reasonable to conclude that the relative inferior PLQY of C/GA/S QDs mainly originated from the slow electron-hole recombination rates, which is caused by the weak quantum confinement effect rather than the existence of the abundant defects within crystals.^[29–32]

To further determine the influence of the interfacial structure on AR process, transient absorption (TA) measurements of the three types of QDs are carried out. The QDs are dissolved by hexane in 1 mm path length cuvettes for the measurements. The samples are pumped by a femtosecond laser

with a pulse width of 100 fs at 355 nm. By changing the pump fluence during the measurement, the single exciton and the multi-exciton carrier dynamics are studied. TA spectra of these QDs at 10 ps are shown in Figure S11, Supporting Information, where the photobleaching (PB) signals can be clearly observed. In order to understand the relationship between the pump fluence and the multi-exciton process in QDs, the average generated electron–hole pair per QD ($\langle N \rangle$) is introduced, which is determined by the expression $\langle N \rangle = j_p \sigma_0$, where j_p is the pump fluence and σ_0 is the absorption cross section.^[10] The pump fluence-dependent PB signal amplitude is used to estimate the value of $\langle N \rangle$, following previous research reports.^[33–41] At long delay time after the QDs are excited, the multi-exciton process completes relatively quickly so that only single exciton condition is remained. The amplitude of the PB signal at this time scale is proportional to the pump fluence. According to the Poisson distribution, the relationship between the amplitude of the PB signal and the pump fluence can be described by the following equation:

$$\Delta A_t \propto [1 - e^{-j\sigma}] \quad (2)$$

Figure 3a demonstrates the data of the PB signal amplitude of C/GA/S QDs at a delay time of 3000 ps as a function of the pump fluence. By fitting the experimental data by the above equation, the value of the absorption cross section is obtained, which can be further used to calculate $\langle N \rangle$. The fitting results of C/S and C/HA/S are shown in Figures S12a and S13a, respectively, Supporting Information.

Figure 3b shows the PB signal kinetics of the C/GA/S QDs sample under different pump fluences. A rapid decay part gradually appears with the increase of $\langle N \rangle$, which is attributed to the generation of multi-excitons. According to the Poisson distribution, when $\langle N \rangle$ is 0.1, more than 99% of the excited

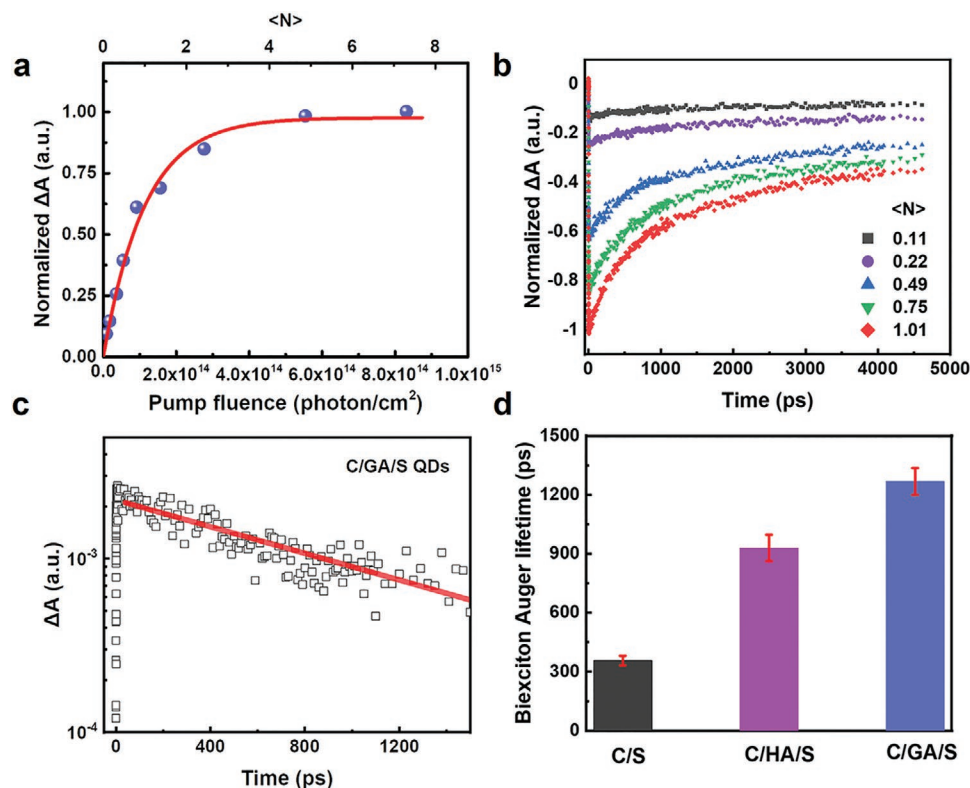


Figure 3. a) PB signal amplitude of C/GA/S at long delay time (3000 ps) as a function of pump fluence. The red solid line is the fitted curve based on the Poisson distribution. b) PB kinetics of C/GA/S QDs at different pump fluence (expressed by $\langle N \rangle$ value). c) Biexciton dynamics of C/GA/S QDs extracted from two PB kinetics ($\langle N \rangle = 0.49$ and $\langle N \rangle = 0.11$) through the subtraction method. The solid red line is the result of fitting through a single exponential decay. d) Biexciton Auger lifetimes of three different types of QDs.

QDs in the sample are in the single exciton state. When $\langle N \rangle$ is 0.5, the percentages for the single-exciton state, the biexciton state and the multi-exciton state in the excited QDs are 77.1%, 19.3%, and 3.6%, respectively, which implies that the single exciton and biexciton processes dominate the PB decay dynamics. The biexciton lifetime can be determined by a subtraction method, which has been used in the previously reported literature.^[10,35–38,42–45] The biexciton decay kinetic of C/GA/S QDs is extracted through subtracting the PB kinetics when $\langle N \rangle = 0.11$ from the PB kinetics when $\langle N \rangle = 0.49$, and the result is shown in Figure 3c. The biexciton decay kinetic can be well-fitted by a single exponential decay, as indicated by the solid red line in Figure 3c, and the fitted biexciton lifetime (τ_{xx}) of C/GA/S QDs is 1131 ± 53.4 ps. Using the same method, the biexciton lifetimes of C/S and C/HA/S QDs are also obtained, which are 345.4 ± 22.6 and 854.3 ± 56.3 ps, respectively (Figures S12 and S13, Supporting Information). The biexciton decay process has two decay channels, namely, the biexciton radiative recombination and the non-radiative AR. Assuming a quadratic scaling of radiative time constant with exciton multiplicity, the biexciton radiative recombination lifetime ($\tau_{xx,r}$) is about a quarter of the single exciton lifetime (τ_x).^[46] Therefore, the biexciton Auger lifetime ($\tau_{xx,A}$) can be calculated through $1/\tau_{xx,A} = 1/\tau_{xx} - 1/\tau_{xx,r}$. The Auger lifetimes of C/S, C/HA/S and C/GA/S QDs are 3572 ± 24.2 , 930 ± 67 , and 1268.2 ± 67.5 ps, respectively (Figure 3d). As we expected, C/GA/S has the longest AR lifetime, which implies that the

controllable engineering alloyed interface can suppress the AR process in QDs effectively.

We further investigate the effects of the shell structures on ASE performance. Figure 4a–c present the schematic diagrams of the three types of QDs and their corresponding approximate shapes of the conduction- and valence-band confinement potentials. Theoretically, the gain threshold is affected by many factors, including the fine energy level structure of single excitons and biexcitons, and the photon energy of pump light.^[5,47] Herein, a laser with 1 ns pulse width at 355 nm (3.49 eV) and 20 Hz repetition rate is selected as the excitation source to exclude the influence of band edge pumping on the gain threshold. We utilize a laser with 1 ns pulse width at 355 nm and 20 Hz repetition rate as the excitation source. The pump intensity-dependent PL spectra for these samples reveal that the spontaneous emission dominates PL spectra at low pump intensities (Figure 4d–f). When the pump fluence exceeds the ASE threshold, both the narrow-linewidth ASE emission peaks in C/S and C/GA/S QDs are appeared at the low-energy shoulder of the corresponding spontaneous emission peaks, due to the attractive (type-I-like) nature of X–X interactions. By contrast, the C/HA/S QDs present the ASE threshold of $16.5 \mu\text{J cm}^{-2}$ pumped by the same laser, which is lower than those of C/S and C/HA/S QDs by a factor of ≈ 10 and 4, respectively. Moreover, it is further reduced to $6.9 \mu\text{J cm}^{-2}$ under the excitation of a femtosecond laser (Figure S14, Supporting Information), which is not only the lowest value from all blue-emitting

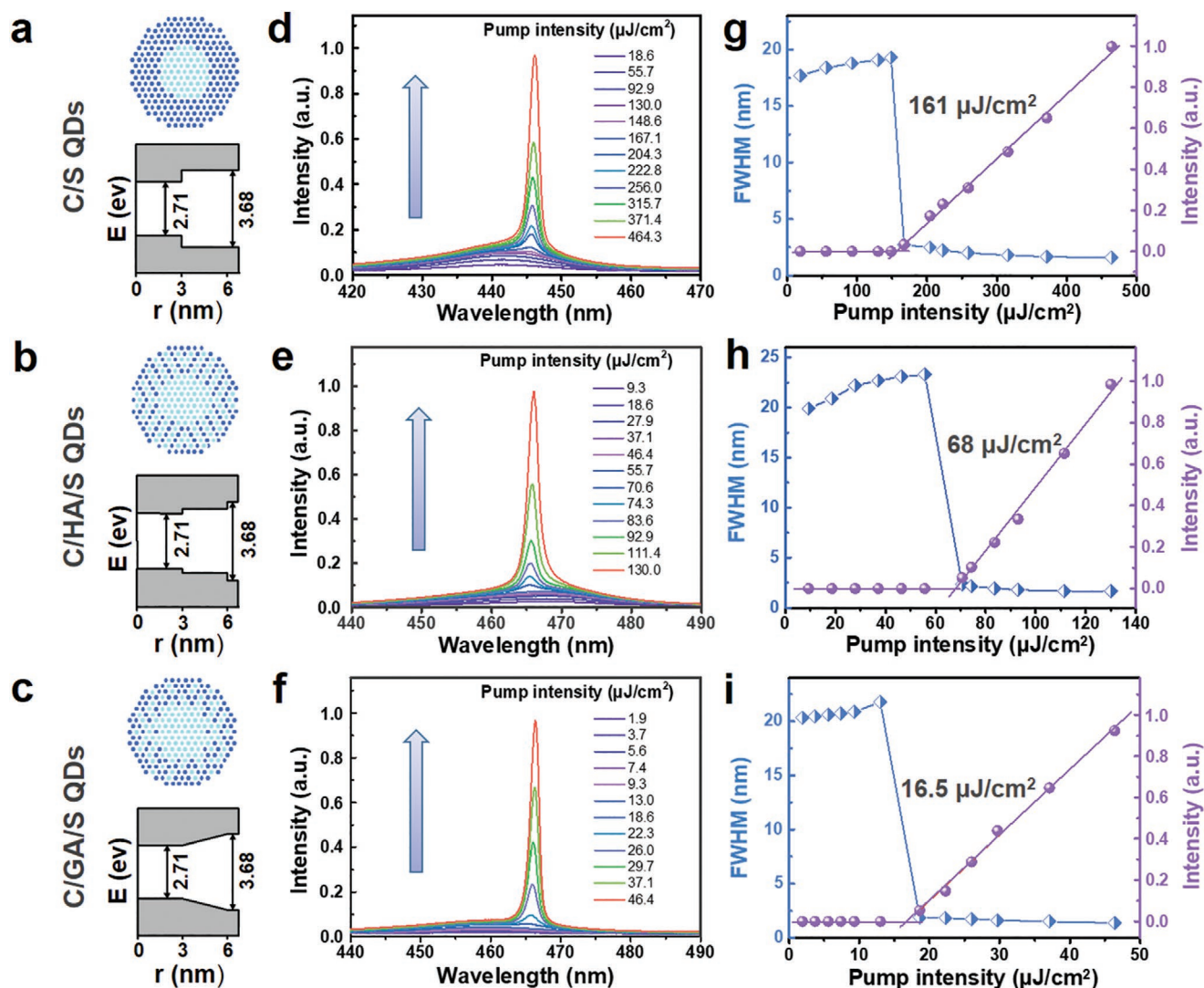


Figure 4. a–c) Structure diagram of C/S, C/HA/S, and C/GA/S QDs, respectively. The corresponding d–f) ASE spectra pumped by a nanosecond laser at different excitation fluences, and g–i) integrated PL intensity and FWHM as a function of the pump intensity.

Table 1. Comparison of representative threshold values reported for different blue-emitting nanocrystals.

Material	Morphology	Cavity type	Laser	Threshold [$\mu\text{J cm}^{-2}$]	Year	Ref.
CdS/ZnS	QDs	Spherical resonator	400 nm/100 fs/1 kHz	3700	2005	[48]
CdSe/ZnCdS	QDs	ASE	400 nm/100 fs/100 kHz	800	2012	[49]
CdSe/ZnCdS	QDs	DFB	355 nm/400 ps/1 kHz	330	2014	[50]
ZnCdS/ZnS	QDs	ASE	400 nm/120 fs/1 kHz	60	2014	[21]
CdSe	NPLs	ASE	400 nm/35 fs/ 100 Hz	50	2015	[51]
CsPb(BrCl) ₃	QDs	ASE	400 nm/100 fs/1 kHz	8–13	2015	[52]
CdS/ZnS	NPLs	ASE	400 nm/120 fs/1 kHz	75	2017	[53]
CsPb(BrCl) ₃	QDs	Vertical cavity	400 nm/100 fs/1 kHz	25.5	2017	[54]
ZnSe	NWs	ASE	400 nm/150 fs/1 kHz	29.8	2019	[55]
ZnCdS/Zn _{1-x} C _x dS/ZnS	QDs	ASE	355 nm/1 ns/20 Hz	16.5	This work	
ZnCdS/Zn _{1-x} C _x dS/ZnS	QDs	ASE	355 nm/100 fs/20 Hz	6.9	This work	

nanocrystals (Table 1), but also comparable to the best values reported in green- and red-emitting QDs. The dramatically enhanced performance can be ascribed to the multifunction of the intermediated gradient alloyed shell, which suppresses the Auger decay, charge tunneling routes, and lattice defects simultaneously.

3. Conclusion

In summary, we have demonstrated that our reactivity balance strategy can precisely engineer the alloyed shell structure. Benefiting from the effect of thick gradient alloyed shell on suppressing the charge tunneling, Auger decay and lattice defects, a long Auger lifetime of 1.3 ns is obtained. Under excitation by a femtosecond laser, the C/GA/S QDs present an ASE threshold of $6.9 \mu\text{J cm}^{-2}$ which is the record value reported in all blue-emitting nanocrystals, and even comparable to the best values from red and green QDs. This work sheds light on the core/shell interface engineering and opens a new path for manipulating the composition and the structure of alloyed shells for diverse optoelectronic applications.

4. Experimental Section

Chemicals: Cadmium oxide (CdO, 99.999%), zinc acetate ($\text{Zn}(\text{Ac})_2$, 99.99%), zinc oxide (ZnO, 99.99%), 1-octadecene (90%, ODE), oleic acid (90%, OA), sulfur (S, 99.99%), DCT (98%) were purchased from Sigma-Aldrich. Acetone (analytical grade), chloroform (analytical grade) and hexane (analytical grade) were purchased from Beijing Chemical Reagent Ltd., China.

Preparation of 0.4 M Zn-Oleate: ZnO (40 mmol), 40 mL OA, and 60 mL ODE were mixed in a 250 mL three-neck flask. The mixture was heated to 140 °C for 1 h with N_2 flowing to remove water and low-boiling point solvents. Then, the mixture was further heated to 310 °C to form golden-yellow transparent solution. Finally, the ZnOA precursor solution was cooled down to 140 °C for further use.

Preparation of 0.2 M Cd-Oleate: CdO (20 mmol), 20 mL OA, and 80 mL ODE were mixed in a 250 mL three-neck flask. The mixture was heated to 140 °C for 1 h with N_2 flowing to remove water and low-boiling point solvents. Then, the mixture was further heated to 260 °C to form golden-yellow transparent solution. Finally, the CdOA precursor solution was cooled down to 80 °C for further use.

Preparation of Sulfur-ODE: 16 mmol sulfur powder was mixed with 24 mL ODE in a 50 mL three-neck flask. Subsequently, the flask was heated up to 160 °C for 30 min to obtain a clear solution. Finally, the S-ODE precursor solution was cooled down to 60 °C for further use.

Preparation of ZnCdS Core QDs: 1 mmol of CdO, 10 mmol of $\text{Zn}(\text{Ac})_2$, 7 mL OA, and 25 mL ODE were mixed in a 100 mL 3-neck flask. This mixture was heated to 140 °C with N_2 flowing. Then, the reaction solution was heated to 310 °C, and 2.4 mL S-ODE was swiftly injected into the flask. The reaction was maintained at 310 °C for 2 h for ZnCdS core QDs growth.

Preparation of ZnCdS/ZnS Core/Shell QDs: For ZnS shell growth, a mixture of 6 mmol DCT and 20 mL ODE was added to the hot reaction solution at a rate of 8 mL h^{-1} by a syringe pump. Subsequently, 25 mL ZnOA and 2 mL DCT were slowly added by syringe pump. After the precursors were added, the reaction was annealed at 310 °C for 1 h, and then allowed to cool to room temperature.

Preparation of ZnCdS/ $\text{Zn}_{0.5}\text{Cd}_{0.5}\text{S}$ /ZnS (C/HA/S QDs) and ZnCdS/ $\text{Zn}_{1-x}\text{Cd}_x\text{S}$ /ZnS Core/Shell QDs (C/GA/S QDs): For ZnS shell growth, a mixture of desired amounts of CdOA and DCT was added into the hot reaction solution at a rate of 8 mL h^{-1} by a syringe pump. Subsequently,

25 mL ZnOA and 2 mL DCT were slowly added by a syringe pump. After the precursors were added, the reaction was further annealed at 310 °C for 1 h, and then allowed to cool to room temperature.

Purification: All the QDs were added into an eightfold volume of hot acetone, and then centrifuged for 5 min at 7500 rpm. The supernatant was discarded, and the precipitate was dispersed in chloroform. The process was repeated another five times.

Characterization: Steady-state and time-resolved PL measurements, including the determination of the absolute PLQYs, were carried out by an Edinburgh FLS920 PL spectrometer. Absorption spectra were performed on a PerkinElmer Lambda 950 UV-vis-NIR spectrometer. XPS measurements were carried out on a ULVAC-PHI 5000 VersaProbe instrument with an achromatic Al $K\alpha$ source (1486.6 eV) and a double pass cylindrical mirror analyzer. TEM measurements were performed on a FEI Tecnai G20 transmission electron microscope. XRD patterns were collected on a Bruker D8 Advance diffractometer with a Cu $K\alpha$ source. Raman spectrum was carried out by a self-built Raman spectrometer. The excitation radiation from a He-Ne laser (532 nm, 200 mW), was directed by an Olympus microscope and focused on samples by a 50× microscope objective. For the ASE measurements, the samples were excited at room temperature with a 355 nm pulse laser (CryLas FTSS355-300-STA) at 20 Hz repetition rate and 1 ns pulse width. The emission spectra were detected by a Newton CCD (model no. DU920P-BU) integrated with a Shamrock spectrometer (model no. SR-750-D1-R). TA was measured by the ExciPro femtosecond TA pump-probe spectrometer (CDP Systems Corp.). The 355 nm excitation laser was transformed through an Astrella ultrafast Ti:sapphire amplifier (Coherent, 800 nm, 1 KHz, 100 fs) by an ultrafast optical parametric amplifier (Coherent Opera Solo).

Supporting Information

Supporting Information is available from the Wiley Online Library or from the author.

Acknowledgements

S.W. and J.Y. contributed equally to this work. The authors gratefully acknowledge financial support from National Natural Science Foundation of China (51675322 and 61735004), Shanghai Science and Technology Committee (19010500600), and National Key Research and Development Program of China (2016YFB0401702).

Conflict of Interest

The authors declare no conflict of interest.

Data Availability Statement

Research data are not shared.

Keywords

alloyed shells, amplified spontaneous emission, Auger recombination, quantum dots, reactivity balance

Received: January 12, 2021

Revised: February 21, 2021

Published online:

- [1] Q. Y. Li, Z. H. Xu, J. R. McBride, T. Q. Lian, *ACS Nano* **2017**, *11*, 2545.
- [2] M. M. Adachi, F. J. Fan, D. P. Sellan, S. Hoogland, O. Voznyy, A. J. Houtepen, K. D. Parrish, P. Kanjanaboos, J. A. Malen, E. H. Sargent, *Nat. Commun.* **2015**, *6*, 8694.
- [3] Y. Shirasaki, G. J. Supran, M. G. Bawendi, V. Bulovic, *Nat. Photonics* **2013**, *7*, 13.
- [4] C. R. Kagan, E. Lifshitz, E. H. Sargent, D. V. Talapin, *Science* **2016**, *353*, aac5523.
- [5] P. Kambhampati, *J. Phys. Chem. Lett.* **2012**, *3*, 1182.
- [6] C. Liao, R. L. Xu, Y. Q. Xu, C. F. Zhang, M. Xiao, L. Zhang, C. G. Lu, Y. P. Cui, J. Y. Zhang, *J. Phys. Chem. Lett.* **2016**, *7*, 4968.
- [7] Y.-S. Park, W. K. Bae, T. Baker, J. Lim, V. I. Klimov, *Nano Lett.* **2015**, *15*, 7319.
- [8] Y. Wang, K. S. Leck, V. D. Ta, R. Chen, V. Nalla, Y. Gao, T. C. He, H. V. Demir, H. D. Sun, *Adv. Mater.* **2015**, *27*, 169.
- [9] H. Shen, S. Wang, H. Wang, J. Niu, L. Qian, Y. Yang, A. Titov, J. Hyvonen, Y. Zheng, L. S. Li, *ACS Appl. Mater. Interfaces* **2013**, *5*, 4260.
- [10] V. I. Klimov, A. A. Mikhailovsky, D. W. McBranch, C. A. Leatherdale, M. G. Bawendi, *Science* **2000**, *287*, 1011.
- [11] J. Cho, Y. K. Jung, J. K. Lee, H. S. Jung, *Langmuir* **2017**, *33*, 3711.
- [12] H. B. Shen, X. W. Bai, A. Wang, H. Z. Wang, L. Qian, Y. X. Yang, A. Titov, J. Hyvonen, Y. Zheng, L. S. Li, *Adv. Funct. Mater.* **2014**, *24*, 2367.
- [13] Q. L. Lin, L. Wang, Z. H. Li, H. N. Shen, L. J. Guo, Y. M. Kuang, H. Z. Wang, L. S. Li, *ACS Photonics* **2018**, *5*, 939.
- [14] F. Cao, S. Wang, F. Wang, Q. Wu, D. Zhao, X. Yang, *Chem. Mater.* **2018**, *30*, 8002.
- [15] S. Wang, J. H. Yu, M. Y. Zhang, D. C. Chen, C. S. Li, R. Chen, G. H. Jia, A. L. Rogach, X. Y. Yang, *Nano Lett.* **2019**, *19*, 6315.
- [16] X. Guo, Y. Kuang, S. Wang, Z. Li, H. Shen, L. Guo, *Nanoscale* **2018**, *10*, 18696.
- [17] B. R. Walsh, J. I. Saari, M. M. Krause, T. G. Mack, R. Nick, S. Coe-Sullivan, P. Kambhampati, *J. Phys. Chem. C* **2016**, *120*, 19409.
- [18] G. E. Cragg, A. L. Efros, *Nano Lett.* **2010**, *10*, 313.
- [19] J. I. Climente, J. L. Movilla, J. Planelles, *Small* **2012**, *8*, 754.
- [20] Y. Wang, K. E. Fong, S. C. Yang, V. D. Ta, Y. Gao, Z. Wang, V. Nalla, H. V. Demir, H. D. Sun, *Laser Photonics Rev.* **2015**, *9*, 507.
- [21] B. Guzelturk, Y. Kelestemur, M. Z. Akgul, V. K. Sharma, H. V. Demir, *J. Phys. Chem. Lett.* **2014**, *5*, 2214.
- [22] W. K. Bae, K. Char, H. Hur, S. Lee, *Chem. Mater.* **2008**, *20*, 531.
- [23] J. Cho, Y. K. Jung, J. K. Lee, *J. Mater. Chem.* **2012**, *22*, 10827.
- [24] A. Mousavi, *Rev. Chim.* **2015**, *66*, 774.
- [25] R. G. Xie, M. Rutherford, X. G. Peng, *J. Am. Chem. Soc.* **2009**, *131*, 5691.
- [26] M. N. T. Hagio, K. Kobayashi, *Carbon* **1989**, *27*, 259.
- [27] C. Duan, W. Luo, T. Jiu, J. Li, Y. Wang, F. Lu, *J. Colloid Interface Sci.* **2018**, *512*, 353.
- [28] M. Cao, L. Li, B. L. Zhang, J. Huang, K. Tang, H. Cao, Y. Sun, Y. Shen, *J. Alloys Compd.* **2012**, *530*, 81.
- [29] X. H. Zhong, R. G. Xie, Y. Zhang, T. Basche, W. Knoll, *Chem. Mater.* **2005**, *17*, 4038.
- [30] J. Wang, Y. T. Long, Y. L. Zhang, X. H. Zhong, L. Y. Zhu, *ChemPhys-Chem* **2009**, *10*, 680.
- [31] X. H. Zhong, Y. Y. Feng, W. Knoll, M. Y. Han, *J. Am. Chem. Soc.* **2003**, *125*, 13559.
- [32] Q. B. Wang, D. K. Seo, *Chem. Mater.* **2006**, *18*, 5764.
- [33] N. Kholmicheva, D. S. Budkina, J. Cassidy, D. Porotnikov, D. Harankahage, A. Boddy, M. Galindo, D. Khon, A. N. Tarnovsky, M. Zamkov, *ACS Photonics* **2019**, *6*, 1041.
- [34] Y. Wang, M. Zhi, Y. Q. Chang, J. P. Zhang, Y. T. Chan, *Nano Lett.* **2018**, *18*, 4976.
- [35] Y. Altintas, K. Gungor, Y. Gao, M. Sak, U. Quliyeva, G. Bappi, E. Mutlugun, E. H. Sargent, H. V. Demir, *ACS Nano* **2019**, *13*, 10662.
- [36] M. J. Li, S. Bhaumik, T. W. Goh, M. S. Kumar, N. Yantara, M. Gratzel, S. Mhaisalkar, N. Mathews, T. C. Sum, *Nat. Commun.* **2017**, *8*, 14350.
- [37] Q. Y. Li, Y. W. Yang, W. X. Que, T. Q. Lian, *Nano Lett.* **2019**, *19*, 5620.
- [38] Y. L. Li, T. Ding, X. Luo, Z. W. Chen, X. Liu, X. Lu, K. F. Wu, *Nano Res.* **2019**, *12*, 619.
- [39] N. Monday, A. De, A. Samanta, *J. Phys. Chem. Lett.* **2018**, *9*, 3673.
- [40] M. Saba, S. Minniberger, F. Quochi, J. Roither, M. Marceddu, A. Gocalinska, M. V. Kovalenko, D. V. Talapin, W. Heiss, A. Mura, G. Bongiovanni, *Adv. Mater.* **2009**, *21*, 4942.
- [41] M. Gramlich, B. J. Bohn, Y. Tong, L. Polavarapu, J. Feldmann, A. S. Urban, *J. Phys. Chem. Lett.* **2020**, *11*, 5361.
- [42] N. Taghipour, S. Delikanli, S. Shendre, M. Sak, M. J. Li, F. Isik, I. Tanriover, B. Guzelturk, T. C. Sum, H. V. Demir, *Nat. Commun.* **2020**, *11*, 3305.
- [43] C. X. She, I. Fedin, D. S. Dolzhenkov, P. D. Dahlberg, G. S. Engel, R. D. Schaller, D. V. Talapin, *ACS Nano* **2015**, *9*, 9475.
- [44] Y. Gao, M. J. Li, S. Delikanli, H. Y. Zheng, B. Q. Liu, C. Dang, T. C. Sum, H. V. Demir, *Nanoscale* **2018**, *10*, 9466.
- [45] J. Lim, Y. S. Park, V. I. Klimov, *Nat. Mater.* **2018**, *17*, 42.
- [46] K. Wu, Y.-S. Park, J. Lim, V. I. Klimov, *Nat. Nanotechnol.* **2017**, *12*, 1140.
- [47] R. R. Cooney, S. L. Sewall, D. M. Sagar, P. Kambhampati, *Phys. Rev. Lett.* **2009**, *102*, 127404.
- [48] Y. Chan, J. S. Steckel, P. T. Snee, J. M. Caruge, J. M. Hodgkiss, D. G. Nocera, M. G. Bawendi, *Appl. Phys. Lett.* **2005**, *86*, 073102.
- [49] C. Dang, J. Lee, C. Breen, J. S. Steckel, S. Coe-Sullivan, A. Nurmikko, *Nat. Nanotechnol.* **2012**, *7*, 335.
- [50] K. Roh, C. Dang, J. Lee, S. T. Chen, J. S. Steckel, S. Coe-Sullivan, A. Nurmikko, *Opt. Express* **2014**, *22*, 18800.
- [51] C. She, I. Fedin, D. S. Dolzhenkov, P. D. Dahlberg, G. S. Engel, R. D. Schaller, D. V. Talapin, *ACS Nano* **2015**, *9*, 9475.
- [52] S. Yakunin, L. Protesescu, F. Krieg, M. I. Bodnarchuk, G. Nedelcu, M. Humer, G. De Luca, M. Fiebig, W. Heiss, M. V. Kovalenko, *Nat. Commun.* **2015**, *6*, 8056.
- [53] B. T. Diroll, D. V. Talapin, R. D. Schaller, *ACS Photonics* **2017**, *4*, 576.
- [54] Y. Wang, X. M. Li, V. Nalla, H. B. Zeng, H. D. Sun, *Adv. Funct. Mater.* **2017**, *27*, 1605088.
- [55] X. J. Li, Q. Wei, K. Y. Wang, S. M. Peng, T. H. Liu, G. C. Xing, Z. K. Tang, *J. Phys. Chem. Lett.* **2019**, *10*, 7516.